Crystallization Characteristics of $CaO-Al_2O_3$-Based Mold Flux and Their Effects on In-Mold Performance during High-Aluminum TRIP Steels Continuous Casting

CHENG-BIN SHI, MYUNG-DUK SEO, JUNG-WOOK CHO, and SEON-HYO KIM

Crystallization behaviors of the newly developed lime-alumina-based mold fluxes for high-aluminum transformation induced plasticity (TRIP) steels casting were experimentally studied, and compared with those of lime-silica-based mold fluxes. The effects of mold flux crystallization characteristics on heat transfer and lubrication performance in casting high-Al TRIP steels were also evaluated. The results show that the crystallization temperatures of lime-alumina-based mold fluxes are much lower than those of lime-silica-based mold fluxes. Increasing B_2O_3 addition suppresses the crystallization of lime-alumina-based mold fluxes, while Na_2O exhibits an opposite effect. In continuous cooling of lime-alumina-based mold fluxes with high B_2O_3 contents and a CaO/Al_2O_3 ratio of 3.3, faceted cuspidine precipitates first, followed by needle-like $CaO{\cdot}B_2O_3$ or $9CaO{\cdot}3B_2O_3{\cdot}CaF_2$. In lime-alumina-based mold flux with low B_2O_3 content (5.4 mass pct) and a CaO/Al_2O_3 ratio of 1.2, the formation of fine CaF_2 takes place first, followed by blocky interconnected $CaO{\cdot}2Al_2O_3$ as the dominant crystalline phase, and rod-like $2CaO{\cdot}B_2O_3$ precipitates at lower temperature during continuous cooling of the mold flux. In B_2O_3-free mold flux, blocky interconnected $3CaO{\cdot}Al_2O_3$ precipitates after CaF_2 and $3CaO{\cdot}2SiO_2$ formation, and takes up almost the whole crystalline fraction. The casting trials show that the mold heat transfer rate significantly decreases near the meniscus during the continuous casting using lime-alumina-mold fluxes with higher crystallinity, which brings a great reduction of surface depressions on cast slabs. However, excessive crystallinity of mold flux causes poor lubrication between mold and solidifying steel shell, which induces various defects such as drag marks on cast slab. Among the studied mold fluxes, lime-alumina-based mold fluxes with higher B_2O_3 contents and a CaO/Al_2O_3 ratio of 3.3 show comparatively improved performance.

DOI: 10.1007/s11663-014-0034-y

I. INTRODUCTION

TRANSFORMATION induced plasticity (TRIP) steels exhibit great applications in automobile industry due to their excellent combination of high strength and superior formability.[1,2] Considering the additional advantages (*i.e.*, improving galvanizability,[2,3] effectively suppressing the surface oxide layer formation induced by high silicon content in the steel,[4,5] and optimizing the TRIP effect during straining[6]) contributed by partial substitution of silicon by aluminum in conventional TRIP steels, high-aluminum TRIP steels have been receiving great attention. However, the change in the chemistry of conventional lime-silica-based mold fluxes resulting from the reduction of SiO_2 in mold flux by aluminum in molten steel has always been one of the extremely serious issues in continuous casting of high-aluminum TRIP steels.[7–10] This variation generally causes the instability of viscosity and other thermophysical properties of mold flux, which has been reported as the principal reasons for various problems during casting of high-Al steels such as breakout, nonuniform heat transfer across mold flux, inadequate lubrication, and poor as-cast slab surface quality, *etc.*[8–10]

In view of the above aspects, it is in urgent need to develop optimal mold fluxes to meet the requirements of high-aluminum steels casting. In recent years, several efforts have been made to explore substitutes for conventional lime-silica-based mold fluxes.[9,11,12] With the main focus on minimization of the interaction between mold flux and molten steel, Blazek *et al.*[9] developed lime-alumina-based mold flux for casting high-aluminum TRIP steel, and the production trials showed that the interaction was markedly reduced and the as-cast slab quality was improved compared with lime-silica-based mold flux, while the mold flux consumption and lubrication remained to be improved. In a more recent study, Cho *et al.*[11] carried out casting trials of TRIP steel containing 1.45 mass pct Al by using the newly developed lime-alumina-based mold fluxes, and the results showed that the lubrication and mold heat

CHENG-BIN SHI, Postdoctoral Fellow, MYUNG-DUK SEO, Ph.D. Candidate, and SEON-HYO KIM, Professor, are with the Department of Materials Science and Engineering, Pohang University of Science and Technology (POSTECH), Pohang 790-784, Republic of Korea. JUNG-WOOK CHO, Research Associate Professor, is with the Graduate Institute of Ferrous Technology, Pohang University of Science and Technology (POSTECH), Pohang 790-784, Republic of Korea. Contact e-mail: jungwook@postech.ac.kr
Manuscript submitted December 9, 2013.
Article published online February 19, 2014.

transfer in casting process and surface quality of slab were improved, compared with that of lime-silica-based mold fluxes. Wu *et al.*[12] reported, based on laboratory experimental results, that the crystalline phases of the developed lime-alumina-based mold fluxes were mainly $12CaO{\cdot}7Al_2O_3$ and $11CaO{\cdot}7Al_2O_3{\cdot}CaF_2$, and suggested that $12CaO{\cdot}7Al_2O_3$ exhibited great potential as a substitute for cuspidine ($3CaO{\cdot}2SiO_2{\cdot}CaF_2$). However, only a few studies regarding lime-alumina-based mold flux have been conducted so far.

In the design and optimization of mold fluxes, great attention should be paid to the crystallization properties of mold flux because they have significant effects on the horizontal heat transfer and lubrication, which are regarded as the most important roles of mold flux in continuous casting.[13] Therefore, lime-alumina-based mold fluxes as the substitute of conventional lime-silica-based mold flux are required to possess some indispensable crystallization properties. Many studies have been conducted to clarify the crystallization characteristics of lime-silica-based mold fluxes using various techniques, including single or double hot thermocouple technique (SHTT/DHTT),[14–20] differential thermal analysis (DTA)[21,22] and confocal scanning laser microscopy (CSLM).[23–26] However, few studies on the crystallization characteristics of lime-alumina-based mold fluxes have been made so far. Wang *et al.*[10] investigated the crystalline phases of the initial lime-silica-based mold flux without B_2O_3 and corresponding spent mold flux taken from mold of ongoing continuous casting of TRIP steel, and their findings showed that the mold flux changed from lime-silica-based to lime-alumina-based mold flux with $NaCaAlSi_2O_7$, CaF_2, and Al_2O_3 as crystalline phases. Zhang *et al.*[24] reported that the crystallization temperature of mold fluxes increased with increasing Al_2O_3/SiO_2 ratio, and CaF_2 precipitated first in mold fluxes and followed by cuspidine ($3CaO{\cdot}2SiO_2{\cdot}CaF_2$) or gehlenite which was dependent on the mass ratio of Al_2O_3/SiO_2. Ryu *et al.*[25] studied experimentally the crystallization behaviors of $CaO\text{-}SiO_2\text{-}CaF_2$ based mold fluxes with various Al_2O_3 addition (3, 15, and 25 mass pct) using CSLM, and found that the increase of Al_2O_3 content in mold flux resulted in the precipitation of CaF_2 during cooling process, and a change in crystalline phase from $3CaO{\cdot}2SiO_2{\cdot}CaF_2$ to $2CaO{\cdot}SiO_2{\cdot}Al_2O_3$. It is still quite necessary to investigate the crystallization behaviors of lime-alumina-based mold fluxes, and their effects on heat transfer and lubrication for further optimizing mold fluxes for continuous casting.

In the previous work,[11] the plant trials showed that the newly developed lime-alumina-based mold fluxes could improve the in-mold performance for high-aluminum TRIP steels casting, compared with the lime-silica-based mold fluxes. As pointed out in that study,[11] further work is still highly needed to reveal the crystallization characteristics of the developed mold fluxes. As a successive work in developing lime-alumina-based mold fluxes, differential scanning calorimetry (DSC), X-ray diffraction (XRD), and field emission scanning electron microscope (FE-SEM) equipped with energy dispersive X-ray spectroscopy (EDS) techniques were used to reveal the crystallization behaviors and determine the crystalline phases of the newly developed lime-alumina-based mold fluxes, and compared with those of lime-silica-based mold fluxes. Continuous cooling transformation (CCT) diagrams of various crystalline phases present in mold fluxes were constructed based on DSC results. Furthermore, the effects of crystallization characteristics of the newly developed lime-alumina-based mold fluxes on their in-mold performance were discussed.

II. EXPERIMENTAL

A. *Sample Preparation*

The present study was carried out on seven types of mold fluxes. The chemical compositions of the mold fluxes are presented in Table I. Mold flux AM1 is one of the currently used commercial mold fluxes for high-aluminum TRIP steels casting, and mold flux AM2 is the lime-silica-based mold flux by adding zirconia into mold flux AM1 with aim to decrease mold heat transfer and improve surface quality of high-aluminum TRIP steel slab. The others are lime-alumina-based mold fluxes. The lime-alumina-based mold fluxes can be categorized into two series. One contains high basicity (mass pctCaO/mass pctSiO_2), with lower to zero B_2O_3 content and a low CaO/Al_2O_3 ratio, *i.e.*, mold fluxes New2 and New3. The other (*i.e.*, mold fluxes New4, New5, and New6) exhibits low basicity, high B_2O_3 content, and a high CaO/Al_2O_3 ratio.

B. *Experimental Procedure*

1. *DSC measurement*

Non-isothermal crystallization characteristics of mold fluxes were first studied using DSC (Netzsch STA 449C; Netzsch Instrument Inc., Germany) technique. The DSC measurements were performed in Ar gas atmosphere (Ar gas flow rate at 60 mL/min). Pure $\alpha\text{-}Al_2O_3$ powder was used as reference material in DSC measurement. The mold flux samples were ground into powder before DSC measurements. For each DSC measurement, approximately 60 mg of sample powder was heated at a constant heating rate of 20 K/min from room temperature to 1573 K (1300 °C) in a platinum crucible with a diameter of 5 mm and a height of 5 mm, and then held for 3 minutes to eliminate bubbles and homogenize its chemical composition. Subsequently, the liquid sample was cooled at a constant cooling rate to room temperature. Four DSC measurements with continuous cooling rates of 5, 10, 15, and 20 K/min were performed for each mold flux, respectively. The DSC signal was recorded automatically during both heating and cooling cycles.

2. *Non-isothermal heat treatment and XRD identification*

Since the mold flux samples after DSC measurements are too small, it is impossible to get crystalline phase determination by XRD. Therefore, a series of continuous

Table I. Chemical Compositions of the Studied Mold Fluxes in the Present Work

Sample No.	Chemical Composition (mass pct)									Viscosity (Pa·s) [1573 K (1300 °C)]	Mass pctCaO/ mass pctSiO_2	Mass pctCaO/ mass pctAl_2O_3
	CaO	SiO_2	Al_2O_3	MnO_2	Na_2O	F	B_2O_3	Li_2O	ZrO_2			
AM1	19.9	36.4	3.8	6.6	11.1	9.8	—	2.1	—	0.180	0.55	5.2
AM2	19.3	35.4	1.5	6.2	10.5	9.3	—	3.0	3.5	0.147	0.55	12.9
New2	30.7	2.2	25.1	—	12.3	15.1	5.4	3.1	—	0.075	13.95	1.2
New3	32.0	2.3	26.2	—	7.4	13.9	—	6.4	—	0.077	13.91	1.2
New4	37.9	9.0	11.4	—	9.0	8.9	16.0	4.9	—	0.055	4.21	3.3
New5	42.6	11.9	13.0	—	4.8	9.3	10.8	4.9	—	0.084	3.58	3.3
New6	37.8	8.9	11.5	—	1.0	8.1	15.0	6.2	—	0.038	4.25	3.3

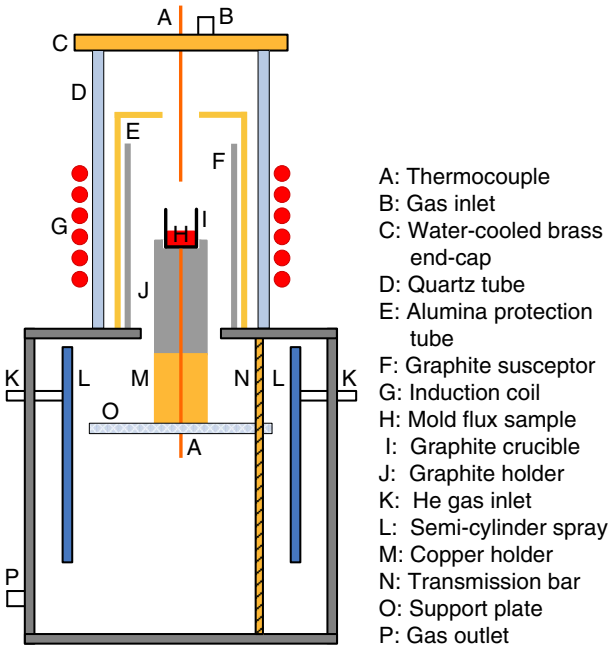

Fig. 1—Schematic diagram of experimental apparatus.

cooling followed by quenching experiments were carried out to prepare mold flux samples for XRD analysis in order to identify the individual crystalline phase corresponding to each exothermic peak on DSC curve. Strict control of a constant continuous cooling rate is critical in these experiments. An induction furnace combined with a controllable quenching system was employed. The experimental apparatus is presented schematically in Figure 1.

The experimental temperature measurement was performed using a two-thermocouple (Pt-30 pctRh/Pt-6 pctRh) technique. One thermocouple was placed in contact with the reaction chamber. The temperature of the furnace reaction chamber was controlled by a proportional-integral-derivative (PID) controller unit connected with this thermocouple. The other thermocouple was attached directly to the bottom of the graphite crucible containing mold flux sample in order to monitor the sample temperature. High purity Ar gas was passed through silica gel, and deoxidized with heated columns of Mg turnings at 823 K (550 °C). Thereafter, the purified Ar gas was introduced into the reaction chamber during the whole experimental process.

Before melting the mold flux sample, the temperature in the hot zone of the induction furnace was elevated to 1673 K (1400 °C) and maintained constant throughout the experiment. Thereafter, a graphite crucible (70 mm in height, 15 mm in inner diameter, 20 mm in outer diameter) containing 7 g of mold flux in each experiment was sent into the even temperature zone of the reaction chamber from the bottom of the induction furnace. The mold flux sample was maintained in the even temperature zone for 30 minutes (timing started when the sample was put into the even temperature zone of reaction chamber) to ensure complete melt and homogenization. This was followed by a continuous cooling at a cooling rate of 10 K/min to the desired target temperature, as listed in Table II, by lowering continuously the graphite crucible containing liquid mold flux from the even temperature zone. The desired target temperature was the temperature below the crystallization end temperature corresponding to each exothermic peak on DSC curve with the cooling rate of 10 K/min. Once reaching the desired temperature, the liquid mold flux placed in the graphite crucible was rapidly lowered into the quenching zone below, and then quenched using He gas. The quenched mold flux samples were ground and analyzed by XRD using Cu-K_α radiation with a scanning rate of 4 deg/min.

3. *FE-SEM/EDS analysis*

The microstructure and crystal compositions of mold flux samples after DSC measurements were determined by FE-SEM/EDS (JSM-7401F, JEOL, Japan). Before FE-SEM/EDS determination, the platinum crucible containing mold flux after DSC measurement was cut along its vertical section at the center of the crucible. Subsequently, the mold flux samples were mounted with epoxy resin and polished. Then, a thin platinum film was coated onto the cross section of the polished sample to enhance the sample electric conductivity.

III. RESULTS AND DISCUSSION

A. *Non-isothermal Crystal Formation and Crystallization Temperatures of Mold Fluxes*

The crystallization temperatures and crystal formation events of mold fluxes at various continuous cooling

Table II. Desired Target Temperatures used in Non-isothermal Heat Treatment Experiments

Exp. No.	Sample No.	Target Temperature [K (°C)]
S1	New2	1033 (760)
S2	New2	938 (665)
S3	New2	873 (600)
S4	New3	1470 (1197)
S5	New3	1173 (900)
S6	New3	673 (400)
S7	New4	923 (650)
S8	New4	788 (515)
S9	New5	923 (650)
S10	New5	793 (520)
S11	New6	923 (650)
S12	New6	673 (400)

rates were determined by DSC. Figure 2 shows the DSC curves of mold fluxes at four different cooling rates, *i.e.*, 5, 10, 15, and 20 K/min, respectively. As shown in Figures 2(a) and (b), no exothermic peak on DSC curves was detected for mold fluxes AM1 and AM2 at four different cooling rates of DSC measurement, except only a single exothermic peak with low intensity for mold flux AM1 at the DSC cooling rate of 5 K/min. These results suggest that no crystal formation event occurs in mold fluxes AM1 and AM2 during continuous cooling process, except for mold flux AM1 with the cooling rate of 5 K/min. It is concluded based on DSC results that the critical cooling rate for crystalline phase formation in mold flux AM1 is between 5 and 10 K/min, and the critical cooling rate for mold flux AM2 is lower than 5 K/min. The ZrO_2 addition of 3.5 mass pct in the lime-silica-based mold flux with low basicity (mass pct-CaO/mass pctSiO_2 = 0.55) might reduce the mold flux crystallization ability, instead of improving the crystallization ability which is the intention of adding ZrO_2 in the design of mold flux AM2. The critical cooling rates of the studied lime-silica-based mold fluxes with low basicity AM1 and AM2 are much lower than that of conventional lime-silica-based mold fluxes determined by other researchers.[15,16] The current findings indicate that it is impossible to form crystals during actual continuous casting process using mold fluxes AM1 and AM2 without considerable change of mold flux chemistry resulting from the reaction between SiO_2 in mold flux and aluminum in molten steel. However, there is a significant increase of mold flux basicity and Al_2O_3 content due to this reduction reaction during production casting of high-Al TRIP steels using mold fluxes AM1 and AM2, which has been revealed in the previous study.[11] This is the very consideration in designing the mold fluxes AM1 and AM2 for high-Al TRIP steels casting.

Figures 2(c) and (d) present the DSC curves of mold fluxes New2 and New3 at various cooling rates. It was observed that there were three exothermic peaks on DSC curves, respectively, indicating the presence of three successive crystallization events. Unlike the crystal formation events that occurred in mold fluxes New2 and New3, only two exothermic peaks on the DSC curves were observed for mold fluxes New4, New5, and New6 at each cooling rate, as shown in Figures 2(e) through (g). These results reveal the occurrence of two-stage crystallization in mold fluxes New4, New5, and New6 during continuous cooling process. The exothermic peaks on DSC curves were designated as P1, P2, and P3, respectively, according to the crystallization order in continuous cooling process. The DSC results show that the exothermic peaks on DSC curves shift toward lower temperature with increasing the cooling rate of DSC measurement. It was observed from Figures 2(e) through (g) that the intensity of the first crystallization exothermic peak was much higher than that of the second exothermic peak on each DSC curve at the same cooling rate. It is noted from Figure 2 that several second or third crystallization exothermic peaks on DSC curves are very broad and obtuse, which suggests that the corresponding crystallization is weak and slow. In addition, the glass transition temperatures on DSC curves were only detected for lime-silica-based mold fluxes AM1 [at about 950 K (677 °C)] and AM2 [at about 750 K (477 °C)], the transition on DSC curve was designated as Pg as shown in Figures 2(a) and (b).

The crystallization temperature of mold flux corresponds to the temperature at which the crystallization just begins in non-isothermal crystallization process. The starting point of the deviation of the exothermic peak from the baseline on DSC curve in continuous cooling process was defined as the crystallization temperature of the corresponding crystalline phase. Similarly, the end point of the deviation of the exothermic peak from the baseline on DSC curve was defined as the crystallization end temperature of the corresponding crystalline phase, indicating that the crystallization of the corresponding crystalline phase was completed. The crystallization temperature of the first crystalline phase precipitated in mold flux correspondingly is the crystallization temperature of the mold flux.

The crystallization temperature combined with the time–temperature profiles recorded in DSC measurement were used to construct CCT diagrams of lime-alumina-based mold fluxes for the cooling rates of 5, 10, 15, and 20 K/min, as shown in Figure 3. It was observed that the crystallization temperatures of the crystalline phases in lime-alumina-based mold fluxes decreased with increasing the continuous cooling rate in DSC measurement. However, the tendency that the crystallization temperature decreases with increasing the DSC cooling rate is weak for the last crystalline phases formed at lower temperatures in the studied lime-alumina-based mold fluxes as shown in Figure 3. This could be due to the fact that the difference in the crystallization kinetics for the last crystalline phases formation induced by the viscosity variations is extremely small, which is because the cooling rate has a negligible effect on mold flux viscosity at lower temperatures. It should be noted that, although the crystallization temperatures of the first crystalline phases precipitated in lime-alumina-based mold fluxes are apparently different, the crystallization temperatures of the last crystalline phases for all the mold fluxes are close to each other [about 900 K (627 °C)].

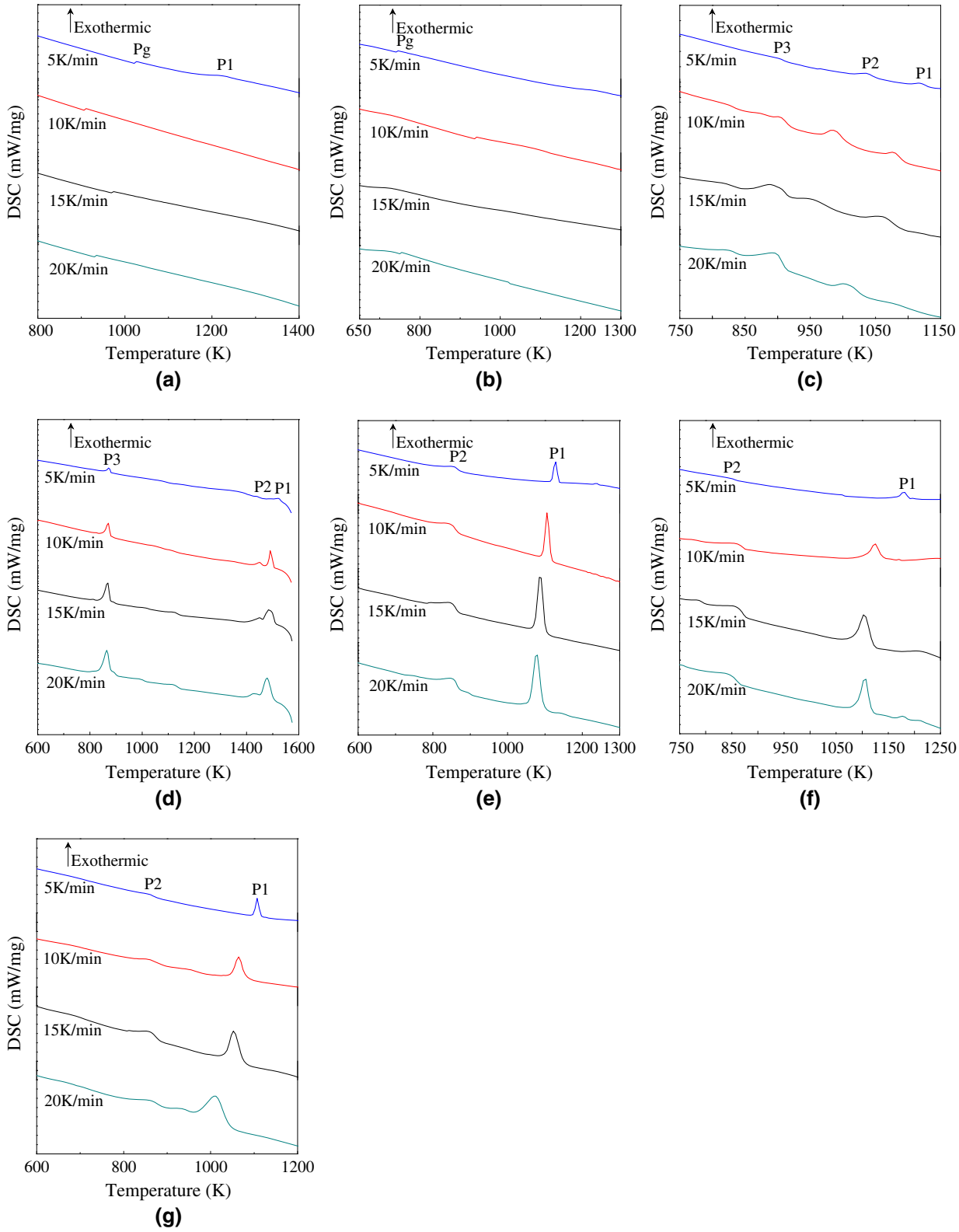

Fig. 2—DSC curves of non-isothermal crystallization of mold fluxes at various cooling rates: (*a*) AM1, (*b*) AM2, (*c*) New2, (*d*) New3, (*e*) New4, (*f*) New5, and (*g*) New6.

Figure 4 presents the CCT diagram of the first crystalline phases precipitated in lime-alumina-based mold fluxes. As pointed out above, the crystallization temperature of the first crystalline phase correspondingly is defined as the crystallization temperature of the mold flux. An obvious difference in crystallization

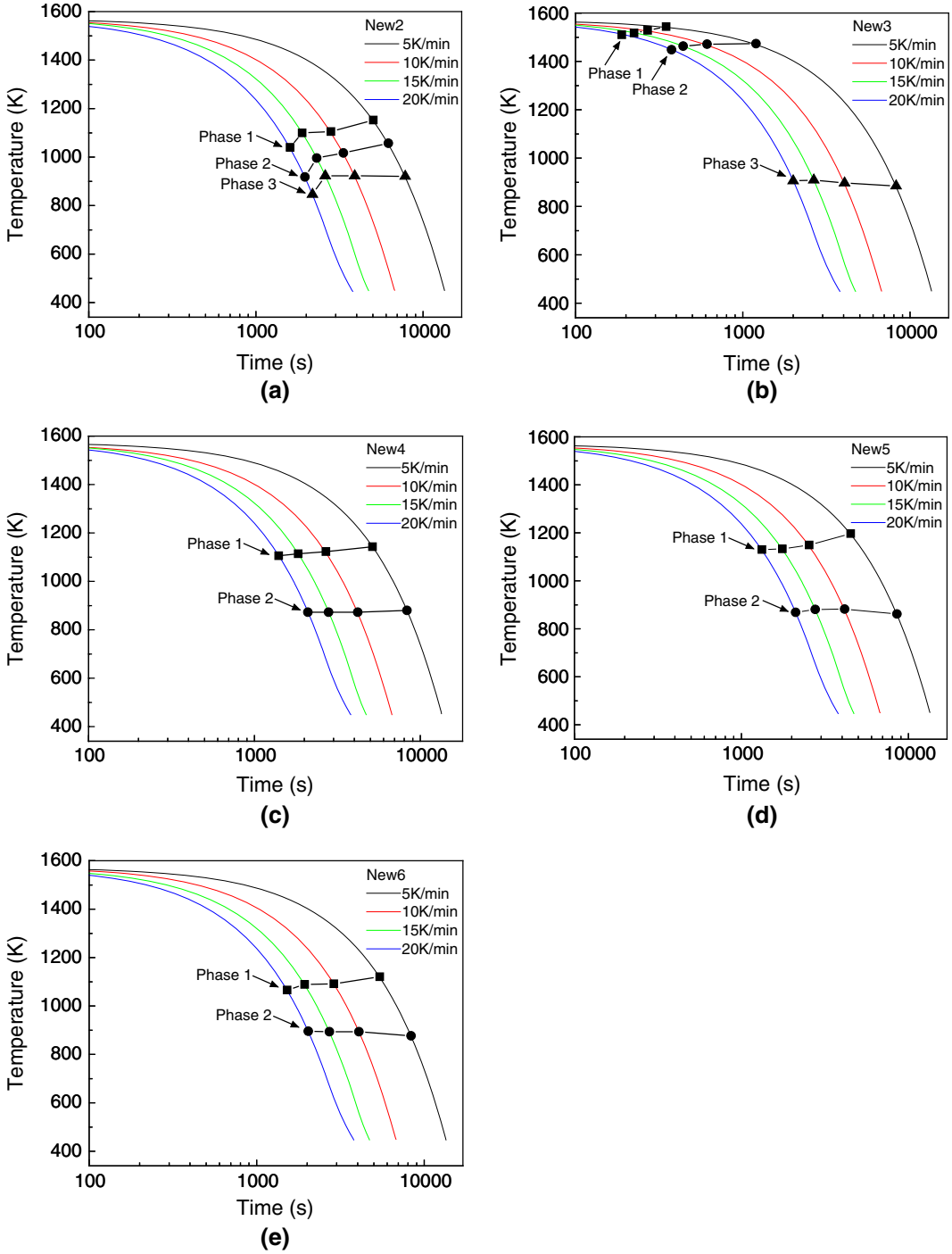

Fig. 3—CCT diagrams of lime-alumina-based mold fluxes: (*a*) New2, (*b*) New3, (*c*) New4, (*d*) New5, and (*e*) New6.

temperatures between B_2O_3-containing and B_2O_3-free lime-alumina-based mold fluxes was observed as shown in Figure 4. It can also be seen from Figure 4 that the crystallization temperature decreases with increasing B_2O_3 addition in the mold fluxes, except for mold flux New2 which contains the highest amount of Na_2O. This exception may be attributed to the fact that the excess Na_2O addition decreases the crystallization of mold flux,[22] although mold flux New2 contains a small amount of B_2O_3. The current finding indicates that the B_2O_3 addition suppresses the crystallization of lime-alumina-based mold fluxes. Lu *et al.*[18] reported a similar observation based on the DHTT image analysis that the crystallization of lime-silica-based mold fluxes was restrained by B_2O_3.

In addition, it should be pointed out that the crystallization temperatures of B_2O_3-containing lime-alumina-based mold fluxes are much lower than that of conventional lime-silica-based mold fluxes at the same cooling rates determined by DSC, *e.g.*, >1300 K

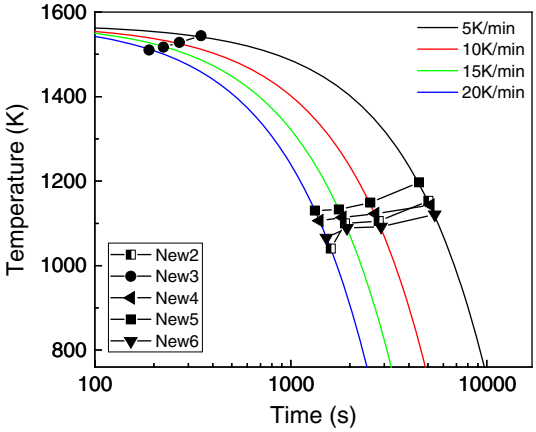

Fig. 4—CCT diagram of the first crystalline phases precipitated in lime-alumina-based mold fluxes.

(1027 °C) reported in the authors' another study,[27] as well as the values reported by other researchers.[21,28] Hao *et al.*[21] determined the crystallization temperatures of conventional lime-silica-based mold fluxes using DTA, and showed that even the crystallization temperatures of cuspidine ($3CaO{\cdot}2SiO_2{\cdot}CaF_2$) crystals as the last crystalline phase in the mold fluxes were higher than 1200 K (927 °C). The crystallization temperatures of $CaO\text{-}SiO_2\text{-}TiO_2$ mold fluxes determined by DTA are above 1200 K (927 °C).[28]

Considering the similar B_2O_3 content in mold fluxes New 4 and New 6 (16.0 and 15.0 mass pct, respectively), it was observed from Figure 4 that the crystallization temperature increased with an increase of Na_2O content in mold flux, which indicated the promotion of the mold flux crystallization by Na_2O addition. This result is consistent with the finding for lime-silica-based mold fluxes reported by other researchers.[17,22] Li *et al.*[17] suggested that the enhancement of mold flux crystallization with Na_2O addition might be attributed to the decrease of viscosity with increasing the Na_2O content in mold flux, which lowered the transfer resistance of ion clusters and energy barrier for crystallization. Watanabe *et al.*[22] pointed out that, it was because Na_2O played a role as network modifier in dividing the silicate flow unit in mold flux and lowering the melting temperature of the mold flux, the crystallization of mold flux was enhanced by appropriate amount of Na_2O addition.

B. *XRD Identification of Crystalline Phases in Mold Fluxes*

Figure 5 shows the XRD patterns of the mold flux samples quenched at the desired target temperatures as listed in Table II. The XRD results are summarized in Table III. The DSC results show three exothermic peaks on each DSC curve for mold flux New2 as shown in Figure 2(c). The crystalline phases corresponding to these exothermic peaks were identified by comparing the XRD patterns of the mold flux samples quenched at the temperatures before and after the crystallization. The XRD analysis revealed that the first crystalline phase in mold flux New2 corresponded to CaF_2 crystal. It was confirmed from the XRD patterns shown in Figure 5(a) that the second and the third exothermic peaks P2 and P3 on DSC curves of mold flux New2 represent $CaO{\cdot}2Al_2O_3$ and $2CaO{\cdot}B_2O_3$ crystals formation, respectively.

Figure 5(b) shows the XRD patterns of the mold flux New3 quenched at the temperatures below the crystallization end temperatures of the second and third exothermic peaks on DSC curve with the cooling rate of 10 K/min, respectively. Since the crystalline phases in the mold flux sample quenched at 1173 K (900 °C) were identified as CaF_2 and $3CaO{\cdot}2SiO_2$, and the crystalline phases in the sample quenched at 673 K (400 °C) were the coexistence of CaF_2, $3CaO{\cdot}2SiO_2$, and $3CaO{\cdot}Al_2O_3$, it can be deduced that the third exothermic peak P3 on DSC curve shown in Figure 2(d) represents the crystallization of $3CaO{\cdot}Al_2O_3$ as the third crystal formation event. It is noted from Figure 2(d) that there is an extremely small spacing between the first exothermic peak and the second exothermic peak on DSC curves, and no clear boundary between the crystallization end temperature of the first exothermic peak and the crystallization starting temperature of the second exothermic peak can be detected. This observation suggests that the interval time between the completion of first crystalline phase formation and the beginning of second crystalline phase precipitation in mold flux New3 is very small during continuous casting process. Furthermore, this is the reason that it is not possible to clarify the crystallization order of CaF_2 and $3CaO{\cdot}2SiO_2$ in mold flux New3 corresponding to the first and second exothermic peaks on DSC curves, respectively, using continuous cooling combined with He gas quenching technique followed by XRD identification of quenched mold flux under the present experimental conditions.

It was confirmed by DSC measurement that two crystal formation events occurred during continuous cooling of mold fluxes New4, New5, and New6. Figure 5(c) shows the XRD patterns of mold flux New4 quenched at the temperatures below the crystallization end temperatures of the first and second exothermic peaks on DSC curve at the cooling rate of 10 K/min. The XRD analysis confirms that the first crystal formation event occurred in mold flux New4 during continuous cooling corresponds to the crystallization of cuspidine ($3CaO{\cdot}2SiO_2{\cdot}CaF_2$), and the second is the crystallization of $9CaO{\cdot}3B_2O_3{\cdot}CaF_2$ crystal.

The XRD patterns of mold fluxes New5 and New6 quenched at two different temperatures are shown in Figures 5(d) and (e). These XRD patterns confirm the presence of only cuspidine ($3CaO{\cdot}2SiO_2{\cdot}CaF_2$) at high quenching temperatures, and the coexistence of cuspidine ($3CaO{\cdot}2SiO_2{\cdot}CaF_2$) and $CaO{\cdot}B_2O_3$ at the low quenching temperatures in mold fluxes New5 and New6. These results indicate that cuspidine ($3CaO{\cdot}2SiO_2{\cdot}CaF_2$) crystals precipitate first, and followed by $CaO{\cdot}B_2O_3$ in continuous cooling of mold fluxes New5 and New6. In addition, it should be pointed out that CaF_2 crystals precipitated only in lime-alumina-based mold fluxes containing higher amount of alumina (*i.e.*, New2 and New3), rather than all the lime-alumina-based mold fluxes. The similar finding showing that

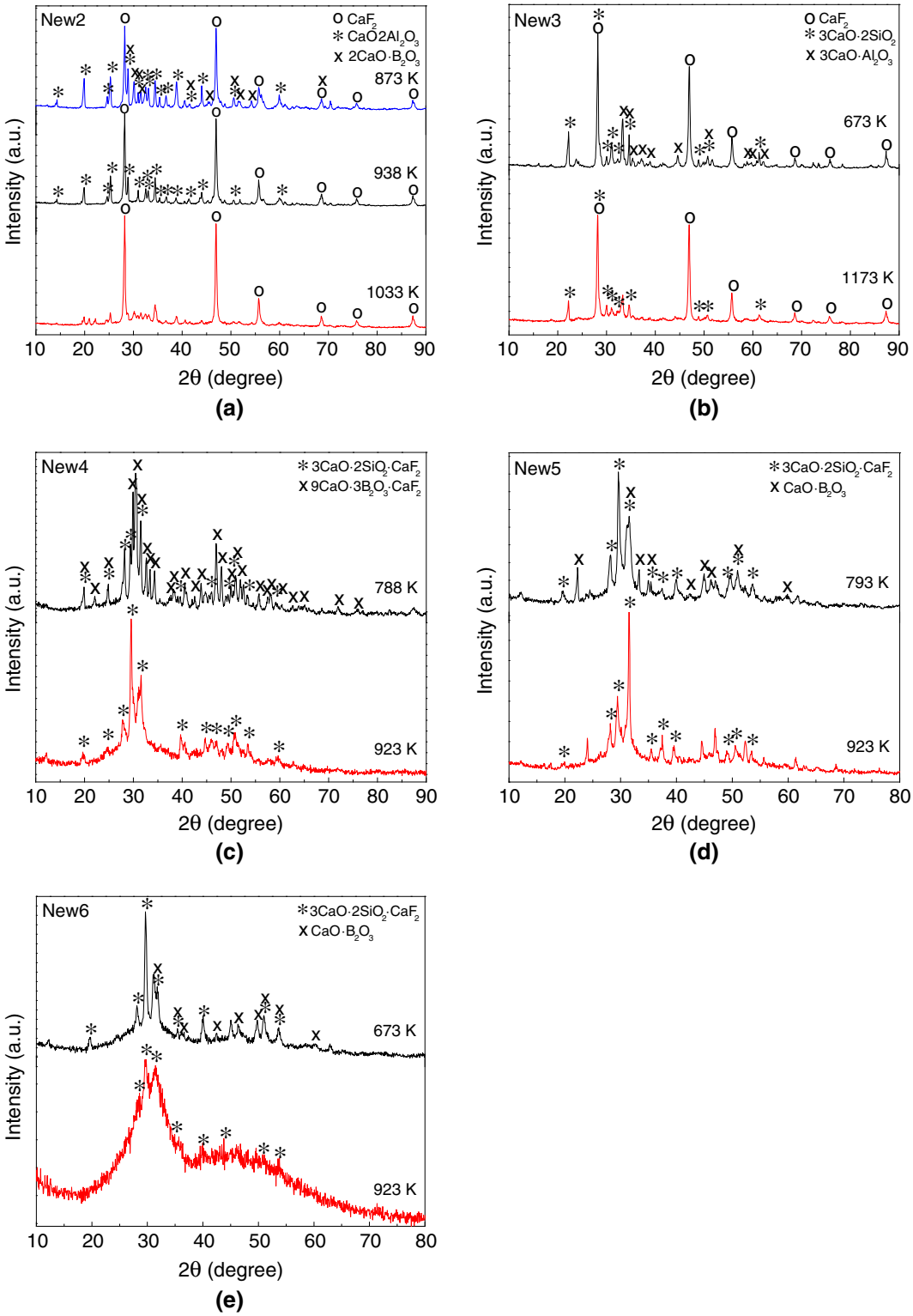

Fig. 5—XRD patterns of the lime-alumina-based mold fluxes quenched at desired target temperatures.

CaF_2 crystal precipitated first, and then followed by other crystal formation events in the high-alumina mold fluxes was also reported by other researchers.[10,24] Zhang *et al.*[24] suggested that alumina addition played a key role in stabilizing CaF_2 crystal in high-alumina mold flux, and consequently CaF_2 crystal precipitated. The further discussion on the order of crystal formation in mold fluxes will be given in Section III–C.

Table III. XRD Analysis Results of Crystalline Phases Present in the Mold Fluxes Quenched at the Desired Target Temperatures

Sample No.	Target Temperature [K (°C)]	Crystalline Phases Identified by XRD
New2	1033 (760)	CaF_2
New2	938 (665)	$CaF_2 + CaO{\cdot}2Al_2O_3$
New2	873 (600)	$CaF_2 + CaO{\cdot}2Al_2O_3 + 2CaO{\cdot}B_2O_3$
New3	1470 (1197)	*
New3	1173 (900)	$CaF_2 + 3CaO{\cdot}2SiO_2$
New3	673 (400)	$CaF_2 + 3CaO{\cdot}2SiO_2 + 3CaO{\cdot}Al_2O_3$
New4	923 (650)	$3CaO{\cdot}2SiO_2{\cdot}CaF_2$
New4	788 (515)	$3CaO{\cdot}2SiO_2{\cdot}CaF_2 + 9CaO{\cdot}3B_2O_3{\cdot}CaF_2$
New5	923 (650)	$3CaO{\cdot}2SiO_2{\cdot}CaF_2$
New5	793 (520)	$3CaO{\cdot}2SiO_2{\cdot}CaF_2 + CaO{\cdot}B_2O_3$
New6	923 (650)	$3CaO{\cdot}2SiO_2{\cdot}CaF_2$
New6	673 (400)	$3CaO{\cdot}2SiO_2{\cdot}CaF_2 + CaO{\cdot}B_2O_3$

*No distinguishable individual crystalline phase can be detected in the sample quenched at this temperature. The detailed discussion on this issue is given in the Section III–B.

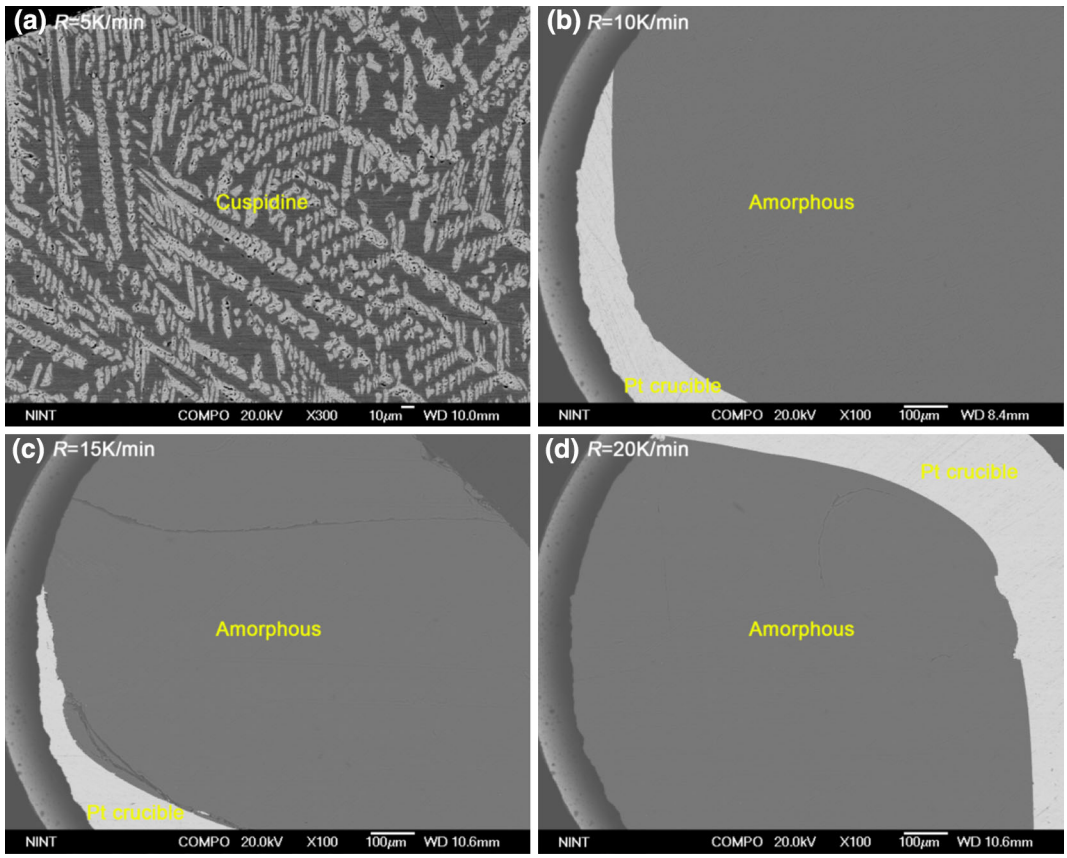

Fig. 6—BSE images of mold flux AM1 after DSC measurement at various cooling rates.

C. *FE-SEM/EDS Observation of Crystalline Phase and Crystal Morphology*

In conventional lime-silica-based mold fluxes, cuspidine ($3CaO{\cdot}2SiO_2{\cdot}CaF_2$) precipitates as primary crystalline phase during mold flux film formation.[13] It has been widely accepted that the crystallization of cuspidine ($3CaO{\cdot}2SiO_2{\cdot}CaF_2$) in conventional lime-silica-based mold fluxes plays a key role in controlling the horizontal heat transfer in continuous casting process.[28] In order to apply lime-alumina-based mold flux system as a substitute for lime-silica-based system in high-Al TRIP steels casting, the crystallization behaviors of the newly developed lime-alumina-based system are required to meet the demands in controlling the horizontal heat transfer and providing adequate lubrication in continuous casting process. To reveal the effect of mold flux crystallization on heat transfer and lubrication, the crystalline phases and crystal morphology

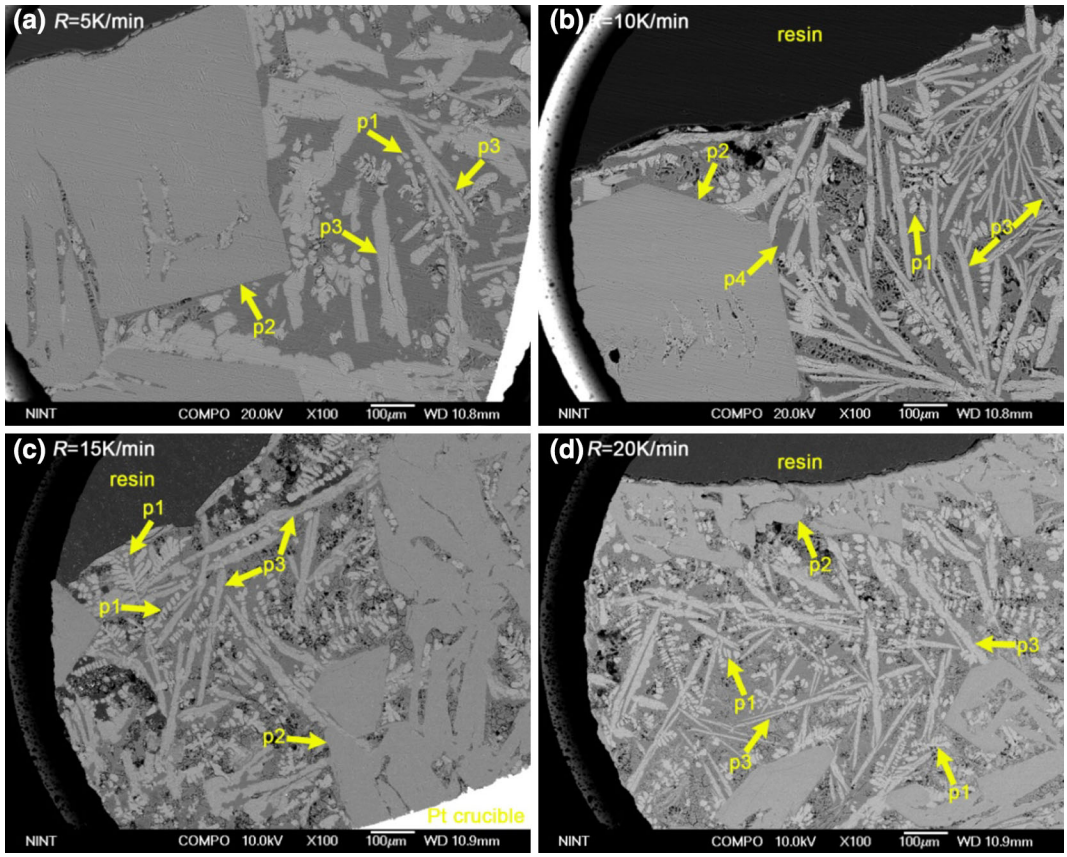

Fig. 7—BSE images of mold flux New2 after DSC measurement at various cooling rates.

characteristics in the newly developed mold fluxes were studied.

Figures 6 through 11 show the FE-SEM back-scattered electron (BSE) images of mold fluxes after DSC measurement with four different continuous cooling rates R, *i.e.*, $R = 5$ K/min, $R = 10$ K/min, $R = 15$ K/min, and $R = 20$ K/min, respectively. It should be pointed out that FE-SEM/EDS analysis revealed that the mold flux samples with the same chemical compositions contained the identical types of crystals even using four different DSC continuous cooling rates. Therefore, only the compositions of crystals precipitated in the mold flux samples with the DSC cooling rate of 10 K/min determined by FE-SEM/EDS are summarized in Table IV.

Figures 6(a) through (d) show the BSE images of mold flux samples AM1 with various DSC cooling rates. Crystals were only found in the sample with the cooling rate of 5 K/min as shown in Figure 6(a), which were identified as cuspidine ($3CaO{\cdot}2SiO_2{\cdot}CaF_2$) by EDS. While the mold flux samples AM1 with the DSC cooling rates of 10, 15, and 20 K/min exhibit amorphous nature as shown in Figures 6(b) through (d), and the same FE-SEM/EDS analysis results were observed for mold flux AM2 with the cooling rates of 5, 10, 15, and 20 K/min, indicating that ZrO_2 addition does not contribute to crystal formation in mold flux AM2. To avoid prolix length of this paper, the BSE images of mold flux AM2 are not presented. These observations are in agreement with the results determined by DSC measurement. It can be seen from Figure 6(a) that cuspidine ($3CaO{\cdot}2SiO_2{\cdot}CaF_2$) crystals are dendritic or rod-like shape, which are, in fact, composed of many fine faceted cuspidine ($3CaO{\cdot}2SiO_2{\cdot}CaF_2$) with regular spacing between the adjacent crystals.

Figures 7(a) through (d) show the BSE images of mold flux samples New2 after DSC measurement at various cooling rates. It was confirmed by FE-SEM/EDS and XRD that there were three kinds of crystalline phases in each sample. The crystals with the blocky morphology are the dominant crystalline phase, which take up the largest crystalline fraction as shown in Figure 7. By combining EDS results with XRD patterns, these crystals were confirmed to be $CaO{\cdot}2Al_2O_3$. It is clear from Figure 7 that the morphology of $CaO{\cdot}2Al_2O_3$ crystals changes from large block with clear angularities to the smaller ones (many of them connect with each other) with increasing the cooling rate of DSC measurement. Second, many $2CaO{\cdot}B_2O_3$ crystals were detected in each sample on the basis of FE-SEM/EDS and XRD analysis. The morphology of $2CaO{\cdot}B_2O_3$ crystals are rod-like, except for only a few $2CaO{\cdot}B_2O_3$ crystals with needle-like shape as shown in Figures 7(b) and (d). In addition, a large amount of very fine CaF_2 crystals with smooth surface were found in each sample, and some of them composed a dendritic shape as shown in Figures 7(a) through (d).

The BSE images of mold flux New3 after DSC measurement at various cooling rates are presented in

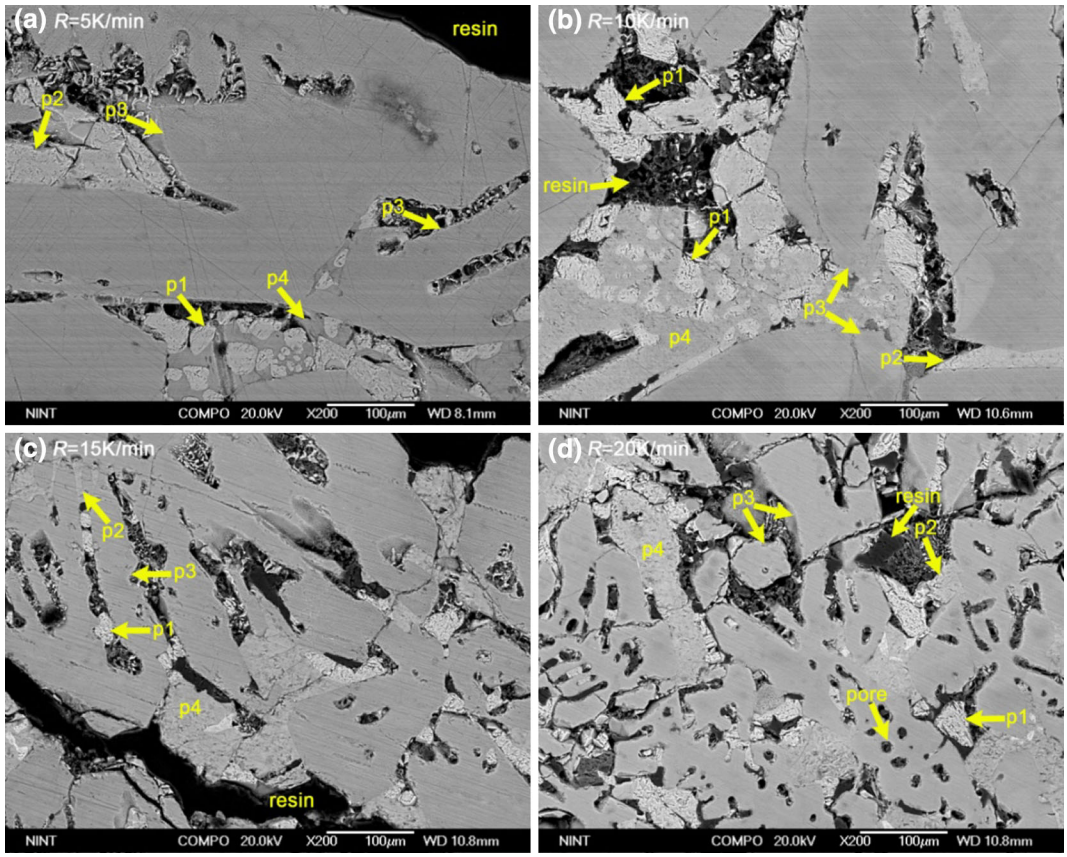

Fig. 8—BSE images of mold flux New3 after DSC measurement at various cooling rates.

Figures 8(a) through (d). It is clear from Figure 8 that the blocky interconnected crystals are the dominant precipitates in mold flux New3. These blocky crystals exhibit large size, and take up almost the whole crystalline fraction in each mold flux sample. A comparison of EDS results and XRD patterns revealed that these blocky crystals are $3CaO{\cdot}Al_2O_3$. Second, a small amount of CaF_2 crystals with smooth surface were found in each sample as shown in Figure 8. In addition, a few small blocky crystals sandwiched between $3CaO{\cdot}Al_2O_3$ crystals can be observed in mold flux New3. These crystals were confirmed to be $3CaO{\cdot}2SiO_2$ by EDS and XRD analysis.

Figures 9 through 11 present the BSE images of mold fluxes New4, New5, and New6 after DSC measurements at various cooling rates, respectively. Figure 9(b) shows the enlarged image of enclosed area of Figure 9(a). Two types of crystals were found in mold fluxes New4, New5, and New6. Although different cooling rates were employed in DSC measurements, needle-like crystals were mainly precipitates in each sample, which were identified as $9CaO{\cdot}3B_2O_3{\cdot}CaF_2$ in mold flux New4, and $CaO{\cdot}B_2O_3$ in mold fluxes New5 and New6 by combining EDS with XRD determination as shown in Tables III and IV. In addition, a large amount of cuspidine ($3CaO{\cdot}2SiO_2{\cdot}CaF_2$) crystals were found (designated as P1 in Figures 9 through 11). The morphology of cuspidine ($3CaO{\cdot}2SiO_2{\cdot}CaF_2$) crystals in mold fluxes New4, New5, and New6 is faceted, except for a few cuspidine ($3CaO{\cdot}2SiO_2{\cdot}CaF_2$) crystals with rod-like morphology in mold flux New5 with the cooling rates of 5 and 15 K/min. The size of both B_2O_3-containing crystals and cuspidine ($3CaO{\cdot}2SiO_2{\cdot}CaF_2$) in mold flux New5 is obviously larger than that in mold fluxes New4 and New6 corresponding to the same cooling rate. No obvious differences in the crystal size and morphology between mold fluxes New4 and New6 were observed.

However, there is a considerable difference in crystal morphology between lime-alumina-based mold fluxes with a low CaO/Al_2O_3 ratio (New2 and New3) and those with a high CaO/Al_2O_3 ratio (New4, New5, and New6). Many blocky interconnected crystals (calcium-aluminate precipitates) with large size which took up the dominant crystalline fraction in the cross-sectional view were detected only in mold fluxes New2 and New3. Furthermore, it is noted that the morphology of cuspidine ($3CaO{\cdot}2SiO_2{\cdot}CaF_2$) crystals formed in the present lime-alumina-based mold fluxes is remarkably different from that in lime-silica-based mold fluxes as shown in Figures 9 through 11, and Figure 6(a). In addition, it should be pointed out that the crystallinity of mold fluxes New2 and especially New3 is considerably higher than that of mold fluxes New4, New5, and New6, which is demonstrated by FE-SEM images shown in Figures 6 through 11.

In the studied lime-alumina-based mold fluxes, calcium fluoride crystals precipitated only in mold fluxes New2 and New3 which contain much higher amount of

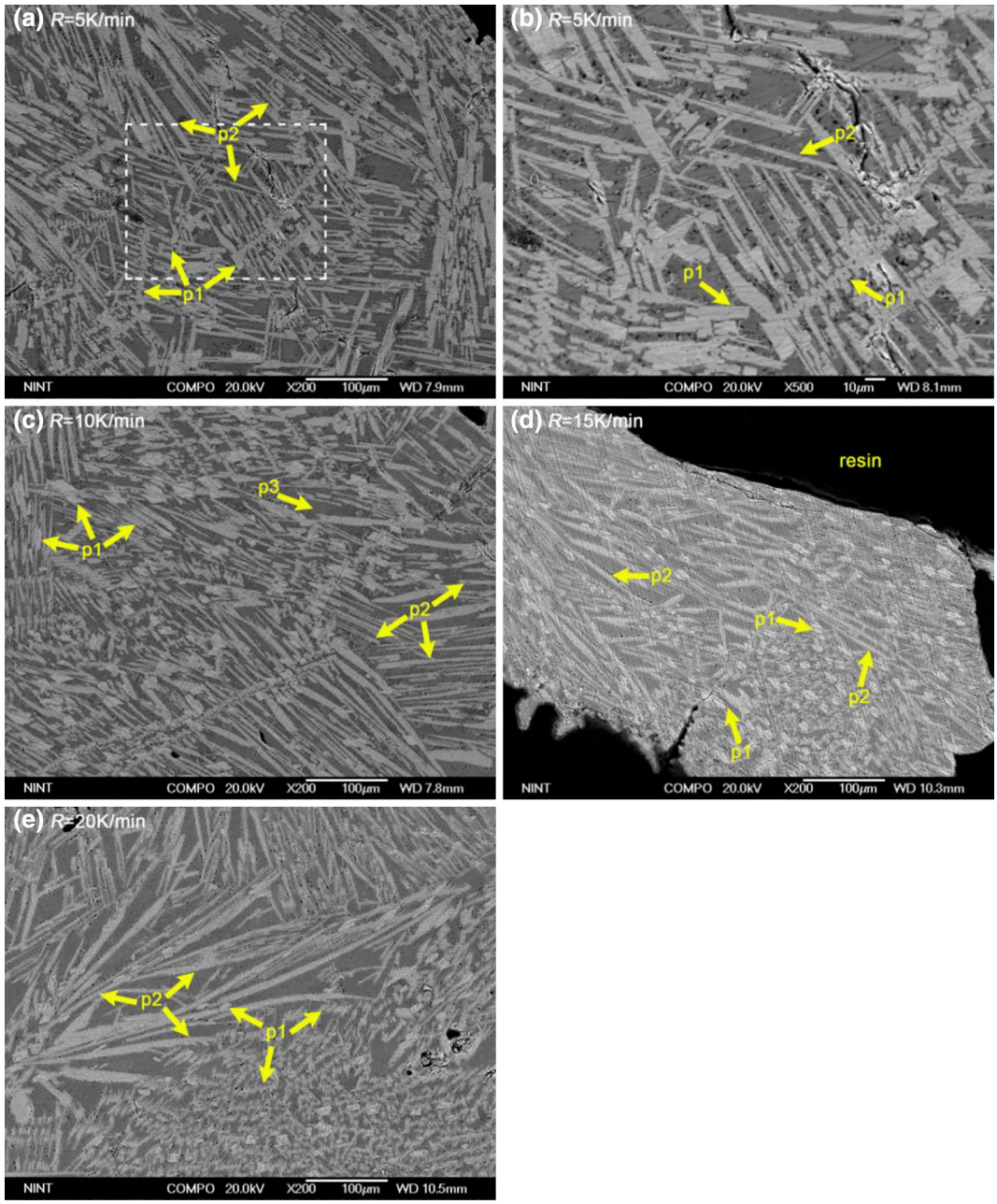

Fig. 9—BSE images of mold flux New4 after DSC measurement at various cooling rates. Note: Fig. (*b*) is enlarged image of the enclosed area of Fig. (*a*).

alumina compared with mold fluxes New4, New5, and New6. The similar finding that the calcium fluoride precipitated in B_2O_3-free lime-alumina-based mold flux taken out of the mold of ongoing continuous casting of TRIP steel was also reported by Wang *et al.*[10]

It can be seen from Figures 7 through 11 that the crystal size in lime-alumina-based mold fluxes decreases with increasing the cooling rates of DSC measurement. It suggests that the increase of continuous cooling rate suppresses the crystallization rate of mold flux. This is attributed to the decrease of the available time required for the crystal growth with increasing the continuous cooling rate. This was the reason that many fine crystals were found in mold fluxes New2, New4, and New6 with the cooling rate of 20 K/min as shown in Figures 7(d), 9(d), 11(d), and 11(e).

Figure 12 shows the microstructure of a typical conventional lime-silica-based mold flux film taken at the mold exit during an ongoing commercial continuous casting of steel. Unlike the newly developed mold fluxes New2, New3, New4, New5, and New6, only cuspidine crystals were found in this conventional lime-silica-based mold flux. The morphology of these cuspidine crystals is faceted which is slightly different from that of the newly developed lime-alumina-based mold fluxes. In the authors' more recent study,[27] it was found that all the crystalline phases in the studied conventional lime-silica-based mold fluxes were cuspidine crystals with

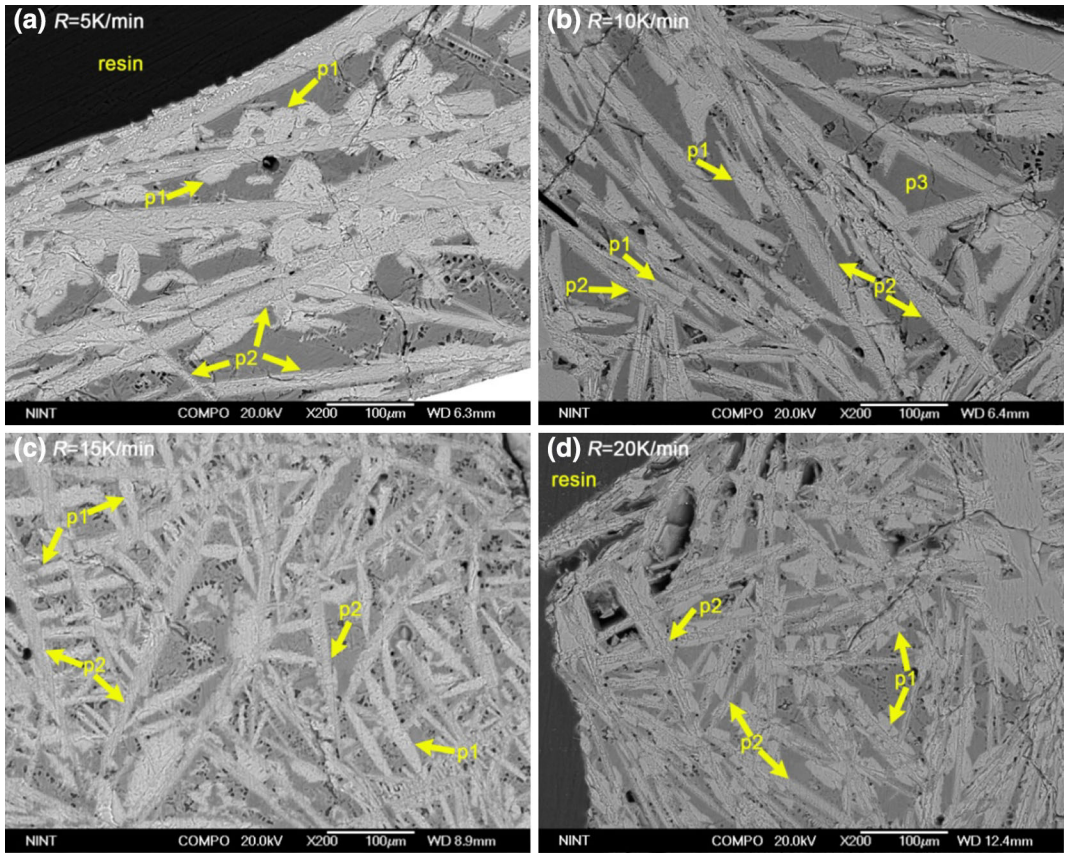

Fig. 10—BSE images of mold flux New5 after DSC measurement at various cooling rates.

dendritic or rod-like morphology which were composed of many fine faceted cuspidine. The crystallinity of the studied conventional lime-silica-based mold fluxes is roughly similar to that of the newly developed mold fluxes, except New3. However, the morphology of crystals in the studied conventional lime-silica-based mold fluxes is apparently different from that observed in the newly developed lime-alumina-based mold fluxes.

It was confirmed that cuspidine ($3CaO{\cdot}2SiO_2{\cdot}CaF_2$) was the first crystalline phase precipitated in lime-alumina-based mold fluxes New4, New5, and New6 during continuous cooling of the mold flux. However, the crystallization temperature of cuspidine in lime-alumina-based mold fluxes New4, New5, and New6 is much lower than that in conventional lime-silica-based mold fluxes at the same continuous cooling rates reported in other studies.[21,27] On the one hand, this is due to the much lower SiO_2 content in mold fluxes New4, New5, and New6 than that in conventional lime-silica-based mold fluxes. As a main component of cuspidine ($3CaO{\cdot}2SiO_2{\cdot}CaF_2$), the lower SiO_2 content is against the precipitation of cuspidine in the mold flux. On the other hand, the difference in crystallization temperature of cuspidine is attributed to the high B_2O_3 contents in mold fluxes New4, New5, and New6 which can act as a network former and enhance glass-formation ability of mold flux, and suppress cuspidine crystallization ability in mold flux.

D. *In-Mold Performance of the Developed Mold Fluxes in Casting High-Al TRIP Steels*

The crystalline phases in mold flux and their crystallization temperatures play an important role in determining the heat transfer and lubrication performance of mold flux in continuous casting operation. These properties of the studied lime-alumina-based mold fluxes are significantly different from those of lime-silica-based AM1 and AM2, as well as conventional lime-silica-based mold fluxes. Therefore, the results of plant trials using the present studied mold fluxes were employed to reveal the effects of mold fluxes crystallization behaviors on in-mold performance of high-Al TRIP steels casting. A 10-ton scale casting pilot caster was employed to cast high-Al TRIP steels containing 1.45 mass pct Al with a casting speed of 0.9 m/min at POSCO, Pohang Works. The heat transfer in casting trials was closely monitored by thermocouples in casting mold. The overall mold heat transfer rate and the mold heat transfer rate near the meniscus in casting process were determined. The surface defects, oscillation marks, and depressions on the cast slabs were evaluated, respectively.

The local mold heat transfer has a direct effect on the initial solidification of molten steel in casting mold. To evaluate the local mold heat transfer rate, factor for temperature difference (FTD) as an indication of the difference of local mold heat transfer rate between the

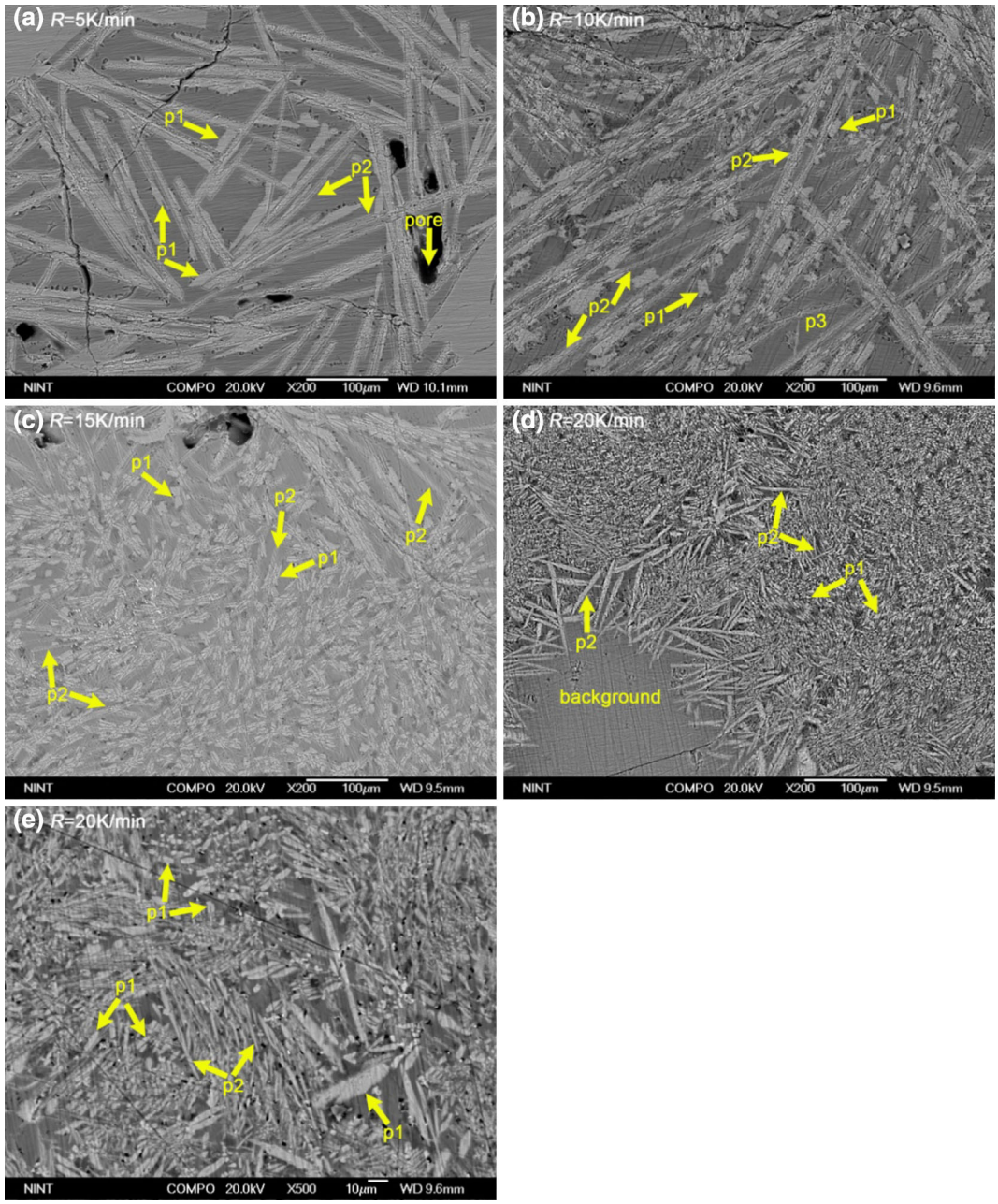

Fig. 11—BSE images of mold flux New6 after DSC measurement at various cooling rates.

positions at 75 and 195 mm below the meniscus was proposed. The larger value of FTD represents the smaller thermal resistance to the heat transfer from molten steel to copper mold during initial stage of casting operation near the meniscus. The detailed derivation of FTD formula has been given elsewhere.[11] The calculated values of FTD in casting trials of high-Al TRIP using the studied mold fluxes are shown in Figure 13. It can be seen that the FTD values for lime-silica-based mold fluxes are significantly greater than that for lime-alumina-based mold fluxes. Meanwhile, the FTD values for lime-alumina-based mold fluxes further decrease by decreasing both CaO/Al_2O_3 ratio and the B_2O_3 content in mold flux. These results are mainly attributed to the higher crystallinity of lime-alumina-based mold fluxes, as discussed in Section III–C.

Figures 14 and 15 show the typical TRIP slab surface after casting trials using various mold fluxes. No apparent difference in surface quality of the slabs produced with mold fluxes AM1 and AM2, New2 and New3 can be observed. Therefore, only the photographs of typical TRIP slab cast using mold fluxes AM1, New2, New4, New5, and New6 are presented in Figures 14 and 15. There are many horizontal and vertical depressions on the slab surface cast with mold flux AM1, and many of these depressions contain open cracks as shown in Figure 14(a). These depressions originated from the irregular solidification in casting mold, which is due to

Table IV. Compositions of Crystals Determined by EDS in the Mold Fluxes After DSC Measurement with the Cooling Rate of 10 K/min, Corresponding to the FE-SEM Images Shown in Figs. 7 Through 11

Fig. No.	Phase	Element (at. pct)						
		B	O	F	Na	Al	Si	Ca
7(b)	P1	—	—	73.7	—	—	—	26.3
	P2	—	51.9	10.5	2.4	21.7	0.7	12.8
	P3	14.5	43.3	18.9	0.5	0.2	3.8	18.8
	P4 (background)	—	55.0	14.5	11.7	10.1	3.6	5.1
8(b)	P1	—	—	73.5	—	—	—	26.5
	P2	—	54.8	13.4	1.2	1.8	9.4	19.5
	P3	—	38.8	26.8	1.9	16.0	0.2	16.3
	P4 (background)	—	40.2	24.0	6.7	1.3	7.4	20.4
9(c)	P1	—	48.2	18.7	0.6	0.4	9.3	22.7
	P2	7.5	63.8	11.1	0.3	—	1.2	16.1
	P3 (background)	—	56.3	9.2	8.7	10.5	7.0	8.3
10(b)	P1	—	46.9	15.4	0.3	0.1	10.2	27.1
	P2	6.3	55.8	13.4	0.2	0.1	1.3	22.9
	P3 (background)	—	54.5	13.3	12.4	8.6	4.8	6.4
11(b)	P1	—	41.3	14.0	—	—	10.0	34.7
	P2	11.9	57.4	7.4	—	—	1.1	22.2
	P3 (background)	—	56.5	11.3	2.5	11.2	5.8	12.7

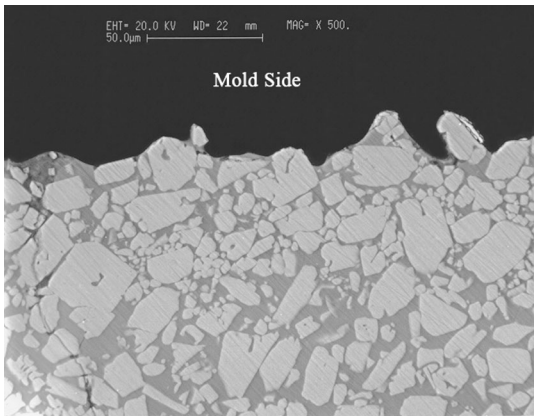

Fig. 12—SEM image of a typical conventional lime-silica-based mold flux film taken at the mold exit during an ongoing commercial continuous casting. (mold flux basicity mass pctCaO/mass pct-SiO_2 = 1.25, all the crystals present in the mold flux film were identified as cuspidine).

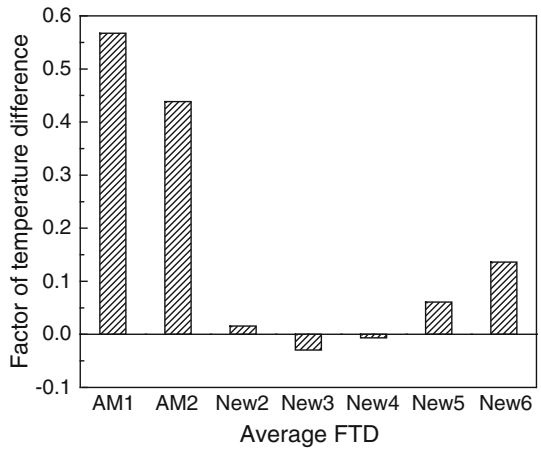

Fig. 13—Average deviation of mold temperature for plant trials using various mold fluxes.

the very low crystallization ability of mold flux AM1 resulting in low thermal resistance and excessive mold heat transfer rate. On the contrary, virtually all the longitudinal and transverse depressions were eliminated when using lime-alumina-based mold fluxes in casting trials. This is mainly attributed to the significant decrease in mold heat transfer rate near the meniscus during continuous casting process, as shown in Figure 13, due to the presence of a crystallized slag film acting as an added resistance for heat transfer.

It is clear from Figure 14 that the oscillation marks on the slab cast using mold flux New2 are not as distinct and straight across the surface of the slab on both the broad and narrow faces as observed on the slab cast with mold flux AM1. But the occurrence of oscillation marks on the slabs increased for the casting trials using mold fluxes New4, New5, and New6, compared with that using mold fluxes New2 and New3. It suggests that the mold fluxes New4, New5, and New6 provide better lubrication than mold fluxes New2 and New3 because of comparatively lower crystallinity due to higher CaO/Al_2O_3 ratio and B_2O_3 addition, as can be seen in Figures 7 through 11.

No drag marks can be observed on the slab surfaces casting using lime-silica-based mold flux as shown in Figure 14(a), which is an indication of adequate lubrication. However, the slabs produced with mold fluxes New2 and New3 did have much more drag marks on the surface than that cast with any of the other mold fluxes, and a few obvious open surface cracks induced by drag marks. This is an evidence of worse lubrication provided by mold fluxes New2 and New3. The plant trials results further suggested that mold fluxes New4, New5, and New6 provided better lubrication as indicated by the significant decrease of drag marks on the cast slab

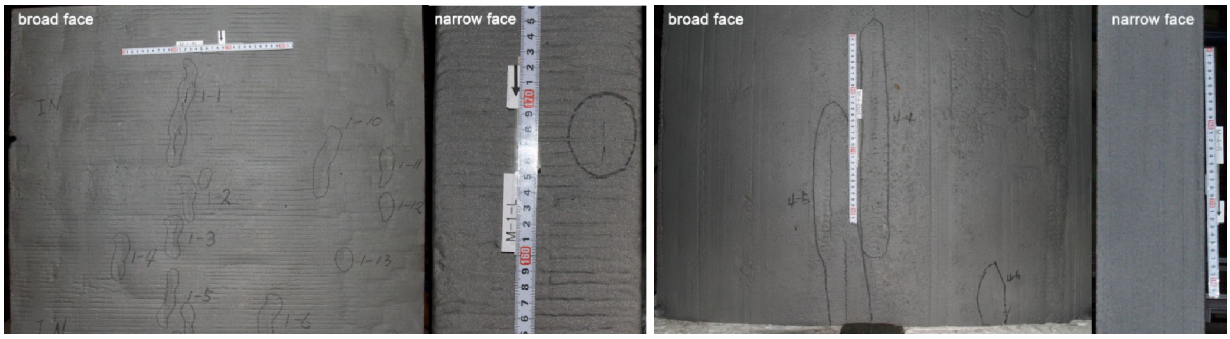

(a) Cast with mold flux AM1 **(b)** Cast with mold flux New2

Fig. 14—Photograph of typical TRIP slab surface after casting trials using mold fluxes AM1 and New2: Note: the casting direction is vertical downward.

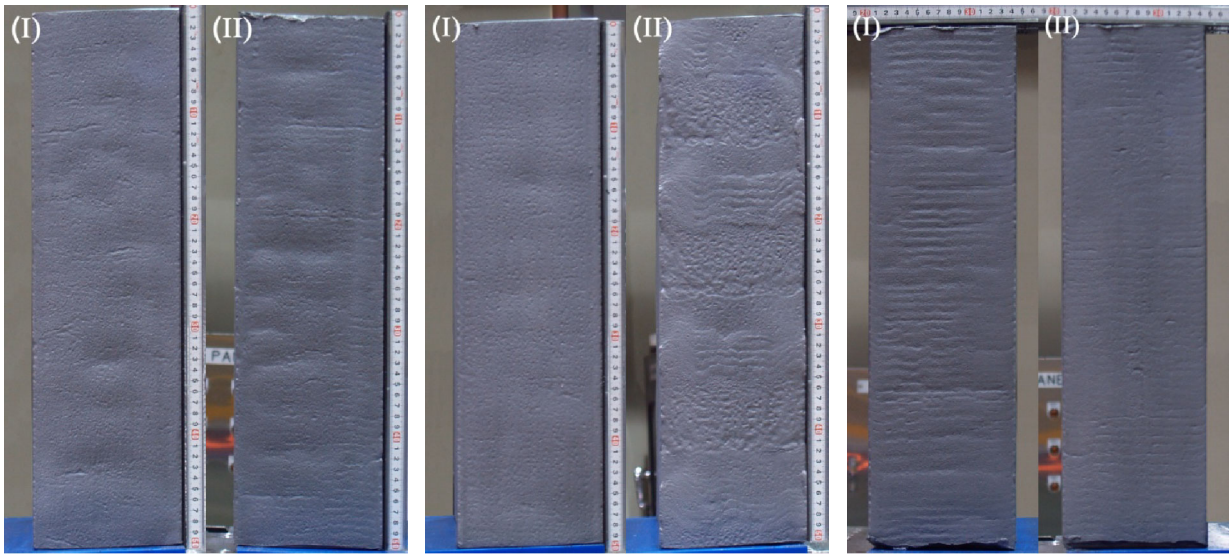

(a) Cast with mold flux New4 **(b)** Cast with mold flux New5 **(c)** Cast with mold flux New6

Fig. 15—Photograph of typical TRIP slab surface after casting trials using various mold fluxes. Note: Figs. (I) and (II) correspond to the slabs with the casting length of 3 to 3.5 m and 7 to 7.5 m, respectively. Figure (II) in Fig. (*a*) was also given in Ref. [11].

compared with mold fluxes New2 and New3. The in-mold performance and slab surface quality in casting trials using mold flux New4 was confirmed to be better than other lime-alumina-based mold fluxes. The present work is expected to provide guidance for further optimizing lime-alumina-based mold fluxes for casting high-aluminum TRIP steels. Some issues are still needed to be improved, such as further improving the lubrication of lime-alumina-based mold fluxes with high B_2O_3 contents and high CaO/Al_2O_3 ratio by optimizing crystal morphology.

IV. CONCLUSIONS

The crystallization behaviors of the newly developed lime-alumina-based mold fluxes and their effects on the horizontal heat transfer and lubrication during production casting of high-aluminum TRIP steels were studied by DSC, XRD, and FE-SEM/EDS techniques, and compared with those of lime-silica-based mold fluxes. The CCT diagrams of the lime-alumina-based mold fluxes were constructed. The conclusions are summarized as follows:

1. The crystallization temperatures of lime-alumina-based mold fluxes are much lower than those of lime-silica-based mold fluxes, and decrease with increasing B_2O_3 content. The addition of B_2O_3 suppresses the crystallization of lime-alumina-based mold fluxes by lowering the crystallization temperature, while Na_2O has an opposite effect.
2. As the current commercial mold fluxes used for high-aluminum TRIP steels casting, the studied lime-silica-based mold fluxes possess extremely low crystallization ability. The crystallinity of lime-alumina-based mold fluxes with a CaO/Al_2O_3 ratio of 1.2 is considerably higher than that of the lime-alumina-based with a CaO/Al_2O_3 ratio of 3.3.

3. In continuous cooling of lime-alumina-based mold fluxes with high B_2O_3 content and a CaO/Al_2O_3 ratio of 3.3, faceted cuspidine precipitates first, followed by needle-like $CaO{\cdot}B_2O_3$ or $9CaO{\cdot}3B_2O_3{\cdot}CaF_2$. In the mold flux with low B_2O_3 content (5.4 mass pct) and a CaO/Al_2O_3 ratio of 1.2, the formation of fine CaF_2 takes place first, followed by blocky interconnected $CaO{\cdot}2Al_2O_3$ as the dominant crystalline phase, and rod-like $2CaO{\cdot}B_2O_3$ precipitates at lower temperature during continuous cooling of the mold flux. In B_2O_3-free lime-alumina-based mold flux, blocky interconnected $3CaO{\cdot}Al_2O_3$ taking up almost the whole crystalline fraction precipitates after a few CaF_2 and $3CaO{\cdot}2SiO_2$ precipitation occurring in a narrow sequential process during continuous cooling.
4. The lubrication of lime-alumina-based mold fluxes without or with low B_2O_3 addition (5.4 mass pct) is poor owing to the presence of blocky interconnected crystals with large size as the dominant crystalline phase. The increase of B_2O_3 addition and CaO/Al_2O_3 ratio significantly improve the lubrication of the lime-alumina-based mold fluxes by reducing the crystallinity of the mold fluxes.
5. The mold heat transfer rate near the meniscus in casting high-aluminum TRIP steels was considerably lowered when using lime-alumina-based mold fluxes in casting trials instead of lime-silica-based mold fluxes. This is caused by the increased crystallinity of lime-alumina-based mold fluxes.
6. Among the studied mold fluxes, the lime-alumina-based mold fluxes with higher B_2O_3 contents and a CaO/Al_2O_3 ratio of 3.3 show the most improved performance, such as TRIP slab surface quality. However, it is highly needed to optimize the crystallization behaviors of the newly developed lime-alumina-based mold fluxes, such as crystal morphology, to cast high-aluminum TRIP steels without defects.

ACKNOWLEDGMENTS

The authors would like to express sincere thanks to Mr. Seung-ho Shin and Mr. Min-su Kim of Graduate Institute of Ferrous Technology, POSTECH for their help in preparing mold flux samples. This work was financially supported by the Global Excellent Technology Innovation (Grant No. 10045029) funded by the Ministry of Trade, Industry & Energy (MOTIE) of Korea.

REFERENCES

1. B. Sauerhammer, D. Senk, E. Schmidt, M. Safi, M. Spiegel, and S. Sridhar: *Metall. Mater. Trans. B*, 2005, vol. 36B, pp. 503–12.
2. M. Gomez, C.I. Garcia, and A.J. Deardo: *ISIJ Int.*, 2010, vol. 50, pp. 139–46.
3. D.W. Suh, S.J. Park, C.S. Oh, and S.J. Kim: *Scripta Mater.*, 2007, vol. 57, pp. 1097–100.
4. M.D. Meyer, D. Vanderschueren, and B.C. De Cooman: *ISIJ Int.*, 1999, vol. 39, pp. 813–22.
5. T.L. Baum, R.J. Fruehan, and S. Sridhar: *Metall. Mater. Trans. B*, 2007, vol. 38B, pp. 287–97.
6. P.J. Jacques, E. Girault, A. Mertens, B. Verlinden, J. Humbeeck, and F. Delannay: *ISIJ Int.*, 2001, vol. 41, pp. 1068–74.
7. J.J. Becker, M.A. Madden, T.T. Natarajan, T.J. Piccone, E.J. Serrano, S.R. Story, S.C. Ecklund-Baker, I.A. Nickerson, and W.K. Schlichting: *AISTech 2005 Conf. Proc.*, vol. II, Association for Iron & Steel Technology, Charlotte, NC, 2005, pp. 99–106.
8. S. Street, K. James, N. Minor, A. Roelant, and J. Tremp: *Iron Steel Technol.*, 2008, vol. 5, pp. 38–49.
9. K. Blazek, H.B. Yin, G. Skoczylas, M. McClymonds, and M. Frazee: *Iron Steel Technol.*, 2011, vol. 8, pp. 232–40.
10. W.L. Wang, K. Blazek, and A. Cramb: *Metall. Mater. Trans. B*, 2008, vol. 39B, pp. 66–74.
11. J.W. Cho, K. Blazek, M. Frazee, H.B. Yin, J.H. Park, and S.W. Moon: *ISIJ Int.*, 2013, vol. 53, pp. 62–70.
12. T. Wu, Q. Wang, S. He, J. Xu, X. Long, and Y. Lu: *Steel Res. Int.*, 2012, vol. 83, pp. 1194–202.
13. K.C. Mills, A.B. Fox, Z. Li, and R.P. Thackray: *Ironmak. Steelmak.*, 2005, vol. 32, pp. 26–34.
14. Y. Kashiwaya, C.E. Cicutti, and A.W. Cramb: *ISIJ Int.*, 1998, vol. 38, pp. 357–65.
15. H. Liu, G. Wen, and P. Tang: *ISIJ Int.*, 2009, vol. 49, pp. 843–50.
16. L. Zhou, W. Wang, F. Ma, J. Li, J. Wei, H. Matsuura, and F. Tsukihashi: *Metall. Mater. Trans. B*, 2012, vol. 43B, pp. 354–62.
17. J. Li, W. Wang, J. Wei, D. Huang, and H. Matsuura: *ISIJ Int.*, 2012, vol. 52, pp. 2220–25.
18. B. Lu, W. Wang, J. Li, H. Zhao, and D. Huang: *Metall. Mater. Trans. B*, 2013, vol. 44B, pp. 365–77.
19. L. Zhou, W. Wang, D. Huang, J. Wei, and J. Li: *Metall. Mater. Trans. B*, 2012, vol. 43B, pp. 925–36.
20. L. Zhou, W. Wang, R. Liu, and B.G. Thomas: *Metall. Mater. Trans. B*, 2013, vol. 44B, pp. 1264–79.
21. Z. Hao, W. Chen, and C. Lippold: *Metall. Mater. Trans. B*, 2010, vol. 41B, pp. 805–12.
22. T. Watanabe, H. Hashimoto, M. Hayashi, and K. Nagata: *ISIJ Int.*, 2008, vol. 48, pp. 925–33.
23. K. Tsutsumti, T. Nagasaka, and M. Hino: *ISIJ Int.*, 1999, vol. 39, pp. 1150–59.
24. Z.T. Zhang, G.H. Wen, J.L. Liao, and S. Sridhar: *Steel Res. Int.*, 2010, vol. 81, pp. 516–28.
25. H.G. Ryu, Z.T. Zhang, J.W. Cho, G.H. Wen, and S. Sridhar: *ISIJ Int.*, 2010, vol. 50, pp. 1142–50.
26. M. Hanao: *ISIJ Int.*, 2013, vol. 53, pp. 648–54.
27. M.D. Seo, C.B. Shi, J.W. Cho, and S.H. Kim: Unpublished research.
28. H. Nakada and K. Nagata: *ISIJ Int.*, 2006, vol. 46, pp. 441–49.